GEOPHYSICS, VOL. 73, NO. 6 (NOVEMBER-DECEMBER 2008); P. S229–S239, 8 FIGS.
10.1190/1.2981241

Isotropic angle-domain elastic reverse-time migration

Jia Yan[1] and Paul Sava[1]

ABSTRACT

Multicomponent data usually are not processed with specifically designed procedures but with procedures analogous to those used for single-component data. In isotropic media, the vertical and horizontal components of the data commonly are taken as proxies for the P- and S-wave modes, which are imaged independently with the acoustic wave equations. This procedure works only if the vertical and horizontal components accurately represent P- and S-wave modes, which generally is not true. Therefore, multicomponent images constructed with this procedure exhibit artifacts caused by incorrect wave-mode separation at the surface. An alternative procedure for elastic imaging uses the full vector fields for wavefield reconstruction and imaging. The wavefields are reconstructed using the multicomponent data as a boundary condition for a numerical solution to the elastic wave equation. The key component for wavefield migration is the imaging condition, which evaluates the match between wavefields reconstructed from sources and receivers. For vector wavefields, a simple component-by-component crosscorrelation between two wavefields leads to artifacts caused by crosstalk between the unseparated wave modes. We can separate elastic wavefields after reconstruction in the subsurface and implement the imaging condition as crosscorrelation of pure wave modes instead of the Cartesian components of the displacement wavefield. This approach leads to images that are easier to interpret because they describe reflectivity of specified wave modes at interfaces of physical properties. As for imaging with acoustic wavefields, the elastic imaging condition can be formulated conventionally (crosscorrelation with zero lag in space and time) and extended to nonzero space and time lags. The elastic images produced by an extended imaging condition can be used for angle decomposition of primary (PP or SS) and converted (PS or SP) reflectivity. Angle gathers constructed with this procedure have applications for migration velocity analysis and amplitude-variation-with-angle analysis.

INTRODUCTION

Seismic processing usually is based on acoustic wave equations, which assume the earth represents a liquid that propagates only compressional waves. Although useful in practice, this assumption is not valid theoretically. Earth materials allow for both compressional- and shear-wave propagation in the subsurface. Shear waves, generated at the source or converted from compressional waves at various interfaces in the subsurface, are detected by multicomponent receivers. Usually, shear waves are stronger at large incidence and reflection angles, often corresponding to large offsets. However, for complex geologic structures near the surface, shear waves can be quite significant, even at small offsets. Conventional single-component imaging ignores shear-wave modes, often leading to incorrect characterization of wave propagation, incomplete illumination of the subsurface, and poor amplitude characterization.

Even when multicomponent data are used for imaging, they are not usually processed with specifically designed procedures. Instead, those data are processed with ad hoc procedures borrowed from acoustic wave-equation imaging algorithms. For isotropic media, a typical assumption is that the recorded vertical and in-plane horizontal components are good approximations for the P- and S-wave modes, respectively, which can be imaged independently. This assumption is not always correct, leading to errors and noise in the images because P- and S-wave modes normally are mixed on all recorded components. Also, because P- and S-wave modes are mixed on all components, true-amplitude imaging is questionable, no matter how accurate the wavefield reconstruction and imaging condition are.

Multicomponent imaging has long been an active research area for exploration geophysicists. Techniques proposed in the literature

Manuscript received by the Editor 4 January 2008; revised manuscript received 16 May 2008; published online 10 November 2008.
[1]Colorado School of Mines, Center for Wave Phenomena, Golden, Colorado, U.S.A. E-mail: jyan@mines.edu; psava@mines.edu.

perform imaging by using time domain using time extrapolation, e.g., by Kirchhoff migration (Kuo and Dai, 1984; Hokstad, 2000) and reverse-time migration (RTM) (Whitmore, 1995; Chang and McMechan, 1986, 1994) adapted for multicomponent data. The reason for working in the time domain, as opposed to the depth domain, is that the coupling of displacements in different directions in elastic wave equations makes it difficult to derive a dispersion relation that can be used to extrapolate wavefields in depth (Clayton and Brown, 1979; Clayton, 1981).

Early attempts at multicomponent imaging used the Kirchhoff framework and separated wave modes on the surface prior to wave-equation imaging (Wapenaar et al., 1987; Wapenaar and Haimé, 1990). Kuo and Dai (1984) perform shot-profile elastic Kirchhoff migration, and Hokstad (2000) performs survey-sinking elastic Kirchhoff migration. Although these techniques represent different migration procedures, they compute traveltimes for PP and PS reflections and they sum data along these traveltime trajectories. This approach is equivalent to distinguishing between PP and PS reflections and applying acoustic Kirchhoff migration separately for each mode. When geology is complex, elastic Kirchhoff migration suffers from drawbacks similar to those of acoustic Kirchhoff migration because ray theory breaks down (Gray et al., 2001).

There are two main difficulties with independently imaging P- and S-wave modes separated on the surface. The first is that conventional elastic migration techniques consider vertical and horizontal components of recorded data as P- and S-wave modes, which is not always accurate, or separate these wave modes on the recording surface using approximations, e.g., polarization (Pestana et al., 1989) or elastic potentials (Etgen, 1988; Zhe and Greenhalgh, 1997) or wavefield extrapolation near the acquisition surface (Wapenaar et al., 1990; Admundsen and Reitan, 1995). Other elastic RTM techniques do not separate wave modes on the surface but reconstruct vector fields using imaging conditions based on ray tracing (Chang and McMechan, 1986, 1994); that are not always robust in complex geology. The second difficulty is that images produced independently from P- and S-modes are hard to interpret together; often they do not line up consistently, requiring image postprocessing such as manual or automatic registration of the images (Gaiser, 1996; Fomel and Backus, 2003; Nickel and Sonneland, 2004).

We advocate an alternative procedure for imaging elastic wavefield data. Instead of separating wavefields into scalar wave modes on the acquisition surface followed by scalar imaging of each mode independently, we use entire vector wavefields for wavefield reconstruction and imaging. The vector wavefields are reconstructed using the multicomponent vector data as boundary conditions for a numerical solution to the elastic wave equation. The key component of such a migration procedure is the imaging condition, which evaluates the match between wavefields reconstructed from the source and receiver. For vector wavefields, a simple component-by-component crosscorrelation between the two wavefields leads to artifacts caused by crosstalk between the unseparated wave modes, i.e., all P- and S-modes from the source wavefield correlate with all P- and S-modes from the receiver wavefield. This problem can be alleviated by using separated elastic wavefields, with the imaging condition implemented as crosscorrelation of wave modes instead of crosscorrelation of the Cartesian components of the wavefield. This approach leads to images that are cleaner and easier to interpret because they represent reflections of single wave modes at interfaces of physical properties.

As for imaging with acoustic wavefields, the elastic imaging condition can be formulated conventionally (crosscorrelation with zero lag in space and time) and extended to nonzero space and time lags. The elastic images produced by an extended imaging condition can be used for angle decomposition of PP and PS reflectivity. Angle gathers have many applications, including migration velocity analysis (MVA) and amplitude-variation-with-angle (AVA) analysis.

Imaging with multicomponent seismic data better represents the physics of wave propagation, and resulting seismic images more accurately characterize the subsurface. Multicomponent images have many applications. For example, they can provide reflection images where the P-wave reflectivity is small, image through gas clouds where the P-wave signal is attenuated, detect fractures through shear-wave splitting, validate bright-spot reflections and provide parameter estimates for this medium, estimate Poisson's ratio, and detect fractures through shear-wave splitting for anisotropic media (Li, 1998; Zhu et al., 1999; Gaiser et al., 2001; Knapp et al., 2001; Simmons and Backus, 2003; Stewart et al., 2003). Assuming no attenuation in the subsurface, converted wave images also have higher resolution than pure-mode images in shallow parts of sections because S-waves have shorter wavelengths than P-waves. Modeling and migrating multicomponent data with elastic migration algorithms enables us to make full use of information provided by elastic data and correctly positioned geologic structures.

This paper presents a method for angle-domain imaging of elastic wavefield data using RTM. To limit the scope, we ignore several practical issues related to data acquisition and preprocessing for wave-equation migration. For example, our methodology ignores the presence of surface waves, e.g., Rayleigh and Love waves; the relatively poor spatial sampling when imaging with multicomponent elastic data, e.g., for OBC acquisition; the presence of anisotropy in the subsurface; and all amplitude considerations related to directionality of the seismic source. All of these issues are important for elastic imaging and need to be part of a practical data-processing application. Instead, we restrict our attention to wave-mode separation after wavefield extrapolation and angle decomposition after the imaging condition.

We begin by summarizing wavefield imaging methodology, focusing on RTM for wavefield multicomponent migration. Then we describe different options for wavefield multicomponent imaging conditions, e.g., based on vector displacements and vector potentials. Finally, we describe the application of extended imaging conditions to multicomponent data and corresponding angle decomposition, illustrating the wavefield imaging techniques with data simulated from the Marmousi2 model (Martin et al., 2002).

WAVEFIELD IMAGING

Seismic imaging is based on numerical solutions to wave equations, which can be classified into ray-based (integral) and wavefield-based (differential) solutions. Kirchhoff migration is a typical ray-based imaging procedure that is efficient computationally but often fails in areas of complex geology, such as subsalt, because the wavefield is distorted severely by lateral velocity variations, leading to complex multipathing. Wavefield imaging works better for complex geology but is more expensive than Kirchhoff migration. Depending on computational time constraints and available resources, different levels of approximation are applied to accelerate imaging, e.g., one way versus two way, acoustic versus elastic, isotropic versus anisotropic.

Despite the complexity of wavefield migration algorithms, any wavefield imaging method can be separated into two parts: wavefield reconstruction followed by application of an imaging condition. For prestack depth migration, source and receiver wavefields must be reconstructed at all locations in the subsurface. The wavefield reconstruction can be conducted using extrapolation in either the depth and or time domain and with different modeling approaches, such as finite differences (Alford et al., 1974; Dablain, 1986), finite elements (Bolt and Smith, 1976), or spectral methods (Seriani and Priolo, 1991; Seriani et al., 1992; Dai and Cheadle, 1996). After reconstructing wavefields with the recorded data as boundary conditions into the subsurface, an imaging condition must be applied at all locations in the subsurface to obtain a seismic image. The simplest imaging conditions are based on crosscorrelation or deconvolution of the reconstructed wavefields (Claerbout, 1971). These imaging conditions can be implemented in the time or frequency domain, depending on the domain in which wavefields have been reconstructed. Here, we concentrate on RTM with wavefield reconstruction and imaging conditions implemented in the time domain.

Reverse-time migration

RTM reconstructs the source wavefield forward in time and the receiver wavefield backward in time. It then applies an imaging condition to extract reflectivity information from the reconstructed wavefields. The advantages of RTM over other depth-migration techniques are that the extrapolation in time does not involve evanescent energy and no dip limitations exist for the imaged structures (McMechan, 1982, 1983; Baysal et al., 1983; Whitmore, 1983). Although conceptually simple, RTM has not been used extensively because of its high computational cost. However, the algorithm is becoming more attractive because of its robustness in imaging complex geology (Boechat et al., 2007; Jones et al., 2007).

McMechan (1982, 1983), Whitmore (1983), and Baysal et al. (1983) first used RTM for poststack or zero-offset data. Underlying poststack RTM is a three-step procedure: (1) reverse the recorded data in time, (2) use the reversed data as sources along the recording surface to propagate the wavefields in the subsurface, and (3) extract the image at zero time, e.g., apply an imaging condition. In poststack RTM, the subsurface reflectors work as exploding reflectors and the wave equation used to propagate data can be applied forward or backward in time by reversing the time axis (Levin, 1984).

Chang and McMechan (1986) apply RTM to prestack data. Prestack RTM reconstructs source and receiver wavefields. The source wavefield is reconstructed forward in time, and the receiver wavefield is reconstructed backward in time. Chang and McMechan (1986, 1994) use an excitation-time imaging condition, where images are formed by extracting the receiver wavefield at the time taken by a wave to travel from the source to the image point. This imaging condition is a special case of the crosscorrelation imaging condition of Claerbout (1971).

Elastic imaging versus acoustic imaging

Multicomponent elastic data often are recorded in land and marine (ocean-bottom) seismic experiments. However, elastic vector wavefields usually are not processed by specifically designed imaging procedures; rather, they are designed by extensions of techniques used for scalar wavefields. Thus, seismic data processing does not take full advantage of the information contained by elastic wavefields. In other words, it does not fully unravel reflections from complex geology or correctly preserve imaging amplitudes and estimate model parameters.

Elastic wave propagation in an infinite, homogeneous, isotropic medium is characterized by the wave equation (Aki and Richards, 2002):

$$\rho\frac{\partial^2\mathbf{u}}{\partial t^2} = \mathbf{f} + (\lambda + 2\mu)\,\nabla(\nabla\cdot\mathbf{u}) - \mu\,\nabla\times\nabla\times\mathbf{u}, \qquad (1)$$

where $\mathbf{u}$ is the vector-displacement wavefield, t is time, ρ is density, $\mathbf{f}$ is the body-source force, and λ and μ are the Lamé moduli. This wave equation assumes a slowly varying stiffness tensor over the imaging space.

The coupling of displacements for different directions in wave equation 1 makes it difficult to derive a dispersion relation to extrapolate wavefields in depth. This makes it natural to extrapolate elastic wavefields in time. For isotropic media, one can process the elastic data by separating wave modes and migrating each mode using methods based on acoustic wave theory or by migrating the whole elastic data set based on equation 1. The elastic wavefield extrapolation using equation 1 is usually performed in time by Kirchhoff migration or RTM, the two main options for elastic imaging in the time domain.

Acoustic Kirchhoff migration is based on diffraction summation, which accumulates data along diffraction curves in the data space and maps them onto the image space. For multicomponent elastic data, Kuo and Dai (1984) discuss Kirchhoff migration for shot-record data. They note that identified PP and PS reflections can be migrated by computing source and receiver traveltimes, using P-wave velocity for the source rays and P- and S-wave velocities for the receiver rays. Hokstad (2000) performs multicomponent anisotropic Kirchhoff migration for multishot, multireceiver experiments; pure and converted mode images are obtained by downward continuation of redatuming viscoelastic vector wavefields and application of a survey-sinking imaging condition to the reconstructed vector wavefields. The wavefield effectively is separated by the Kirchhoff integral, which handles both P- and S-waves; however, this technique fails in areas of complex geology where ray theory breaks down.

Elastic RTM has the same components as acoustic RTM: reconstruct source and receiver wavefield and apply an imaging condition. The source and receiver wavefields are reconstructed by forward and backward propagation in time with various modeling approaches. For acoustic RTM, wavefield reconstruction is done with the acoustic wave equation using the recorded scalar data as boundary conditions. In contrast, for elastic RTM, reconstruction is done with the elastic wave equation, using the recorded vector data as boundary conditions.

Because pure and converted mode reflections are mixed on all components of recorded data, images produced with reconstructed elastic wavefields are characterized by crosstalk as a result of the interference of various wave modes. To obtain images with clear physical meanings, most imaging conditions separate wave modes because they are mixed in all components of the data. There are two potential approaches to separate wavefields and image elastic seismic wavefields. The first is to separate P- and S-modes on the acquisition surface from the recorded elastic wavefields. This procedure involves approximations for the propagation path and polarization direction of the recorded data or reconstructing the seismic wavefields

in the vicinity of the acquisition surface by a numerical solution of the elastic wave equation, followed by wavefield separation of scalar and vector potentials using Helmholtz decomposition (Etgen, 1988; Zhe and Greenhalgh, 1997). An alternative data decomposition using P and S potentials is to reconstruct wavefields in the subsurface using the elastic wave equation, then decompose the wavefields into P- and S-wave modes. This is followed by forward extrapolation of the separated wavefields back to the surface using the acoustic wave equation with the appropriate propagation velocity for the various wave modes (Sun et al., 2006) by conventional procedures used for scalar wavefields.

The second option is to extrapolate subsurface wavefields using a numerical solution to the elastic wave equation and then to apply an imaging condition that extracts reflectivity information from the source and receiver wavefields. If extrapolation is implemented by finite-difference methods (Chang and McMechan, 1986, 1994), this procedure is known as elastic RTM and is conceptually similar to acoustic RTM (Baysal et al., 1983), which is used more frequently in seismic imaging.

Many imaging conditions can be used for RTM. Elastic imaging conditions are more complex than acoustic imaging conditions because source and receiver wavefields are vector fields. Different elastic imaging conditions have been proposed for extracting reflectivity information from reconstructed elastic wavefields. Hokstad et al. (1998) use elastic RTM with Lamé potential methods. Chang and McMechan (1986) use the excitation-time imaging condition, which extracts reflectivity information from extrapolated wavefields at traveltimes from the source to image positions computed by ray tracing. Ultimately, these imaging conditions represent special cases of a more general type of imaging condition that involves time crosscorrelation or deconvolution of source and receiver wavefields at every location in the subsurface.

CONVENTIONAL ELASTIC IMAGING CONDITIONS

For vector elastic wavefields, the crosscorrelation imaging condition needs to be implemented on all components of the displacement field. The problem with this condition is that the source and receiver wavefields contain a mix of P- and S-wave modes that crosscorrelate independently, hampering interpretation of migrated images. An alternative is to perform wavefield separation of scalar and vector potentials after wavefield reconstruction in the imaging volume but before the imaging condition and then crosscorrelate pure modes from the source and receiver wavefields, as suggested by Dellinger and Etgen (1990) and illustrated by Cunha Filho (1992).

Imaging with scalar wavefields

As mentioned, assuming single scattering in the earth (Born approximation), a conventional imaging procedure consists of two components: wavefield extrapolation and imaging. Wavefield extrapolation reconstructs in the imaging volume the seismic wavefield using the recorded data on the acquisition surface as a boundary condition. Imaging extracts reflectivity information from the extrapolated source and receiver wavefields.

Assuming scalar recorded data, wavefield extrapolation using a scalar wave equation reconstructs scalar source and receiver wavefields $u_s(\mathbf{x},t)$ and $u_r(\mathbf{x},t)$ at every location $\mathbf{x}$ in the subsurface. Using the extrapolated scalar wavefields, a conventional imaging condition (Claerbout, 1985) can be implemented as crosscorrelation at zero lag time:

$$I(\mathbf{x}) = \int u_s(\mathbf{x},t)u_r(\mathbf{x},t)dt. \tag{2}$$

Here, $I(\mathbf{x})$ denotes a scalar image obtained from scalar wavefields, and $u_s(\mathbf{x},t)$ and $u_r(\mathbf{x},t)$, $\mathbf{x} = \{x,y,z\}$ represent Cartesian space coordinates, and t represents time.

Imaging with vector displacements

Assuming vector recorded data, wavefield extrapolation using a vector wave equation reconstructs $\mathbf{u}_s(\mathbf{x},t)$ and $\mathbf{u}_r(\mathbf{x},t)$ at every location $\mathbf{x}$ in the subsurface. Here, $\mathbf{u}_s$ and $\mathbf{u}_r$ represent displacement fields reconstructed from data recorded by multicomponent geophones at the surface boundary. Using the vector-extrapolated wavefields $\mathbf{u}_s = \{u_{sx},u_{sy},u_{sz}\}$ and $\mathbf{u}_r = \{u_{rx},u_{ry},u_{rz}\}$, an imaging condition can be formulated as a straightforward extension of equation 2 by crosscorrelating all combinations of components of the source and receiver wavefields. Such an imaging condition for vector displacements can be formulated mathematically as

$$I_{ij}(\mathbf{x}) = \int u_{si}(\mathbf{x},t)u_{rj}(\mathbf{x},t)dt, \tag{3}$$

where the quantities u_i and u_j stand for the Cartesian components x,y,z of the vector source and receiver wavefields $\mathbf{u}(\mathbf{x},t)$. For example, $I_{zz}(\mathbf{x})$ represents the image component produced by crosscorrelating the z-components of the source and receiver wavefields, and $I_{zx}(\mathbf{x})$ represents the image component produced by crosscorrelating the z-component of the source wavefield with the x-component of the receiver wavefield. In general, an image produced with this procedure has nine components at every location in space.

The main drawback of applying this condition is that the wavefield used for imaging contains a combination of P- and S-wave modes. Those wavefield vectors interfere with one another in the imaging condition because the P- and S-components are not separated in the extrapolated wavefields. The crosstalk between various components of the wavefield creates artifacts and makes it difficult to interpret the images in terms of pure wave modes, e.g., PP or PS reflections. This situation is similar to imaging with acoustic data contaminated by multiples or other coherent noise that are mapped in the subsurface using an incorrect velocity.

Imaging with scalar and vector potentials

An alternative to the elastic imaging condition from equation 3 is to separate the extrapolated wavefield into P and S potentials after extrapolation and to image using crosscorrelations of the vector and scalar potentials (Dellinger and Etgen, 1990). Scalar and vector potentials can be separated by Helmholtz decomposition, which applies to any vector field $\mathbf{u}(\mathbf{x},t)$:

$$\mathbf{u} = \nabla \Phi + \nabla \times \mathbf{\Psi}, \tag{4}$$

where $\Phi(\mathbf{x},t)$ represents the scalar potential of the wavefield $\mathbf{u}(\mathbf{x},t)$, $\mathbf{\Psi}(\mathbf{x},t)$ represents the vector potential of the wavefield $\mathbf{u}(\mathbf{x},t)$, and $\nabla \cdot \mathbf{\Psi} = 0$. For isotropic elastic wavefields, equation 4 is not used directly in practice, but the scalar and vector components are obtained indirectly by applying the divergence ($\nabla \cdot$) and curl ($\nabla \times$) operators to the extrapolated elastic wavefield $\mathbf{u}(\mathbf{x},t)$:

$$P = \nabla \cdot \mathbf{u} = \nabla^2 \Phi, \quad (5)$$

$$\mathbf{S} = \nabla \times \mathbf{u} = -\nabla^2 \Psi. \quad (6)$$

For isotropic elastic fields far from the source, quantities P and $\mathbf{S}$ describe compressional and transverse components of the wavefield, respectively (Aki and Richards, 2002). In two dimensions, $\mathbf{S}$ corresponds to SV-waves polarized in the propagation plane.

Using the separated scalar and vector components, we can formulate an imaging condition that combines various incident and reflected wave modes. The imaging condition for vector potentials can be formulated mathematically as

$$I_{ij}(\mathbf{x}) = \int \alpha_{si}(\mathbf{x},t)\alpha_{rj}(\mathbf{x},t)dt, \quad (7)$$

where the quantities α_i and α_j stand for the various wave modes $\alpha = \{\mathrm{P},\mathrm{S}\}$ of the vector source and receiver wavefields $\mathbf{u}(\mathbf{x},t)$. For example, $I_{\mathrm{PP}}(\mathbf{x})$ represents the image component produced by crosscorrelating the P-wave mode of the source and receiver wavefields, and $I_{\mathrm{PS}}(\mathbf{x})$ represents the image component produced by crosscorrelating the P-wave mode of the source wavefield with the S-wave mode of the receiver wavefield. In isotropic media, an image produced with this procedure has four independent components at every location in space, similar to the image produced by crosscorrelating the various Cartesian components of the vector displacements. However, in this case, the images correspond to various combinations of incident P- or S-waves and reflected P- or S-waves, thus having clear physical meaning and being easier to interpret for physical properties.

EXTENDED ELASTIC IMAGING CONDITIONS

The conventional imaging condition from equation 2 uses zero space and time lags of the crosscorrelation between the source and receiver wavefields. This imaging condition represents a special case of a more general form of imaging condition, sometimes referred to as an extended imaging condition (Sava and Fomel, 2006b):

$$I(\mathbf{x},\boldsymbol{\lambda},\tau) = \int u_s(\mathbf{x}-\boldsymbol{\lambda},t-\tau)u_r(\mathbf{x}+\boldsymbol{\lambda},t+\tau)dt, \quad (8)$$

where $\boldsymbol{\lambda} = \{\lambda_x,\lambda_y,\lambda_z\}$ and τ stand for crosscorrelation lags in space and time, respectively. The imaging condition from equation 2 is equivalent to the extended imaging condition from equation 8 for $\boldsymbol{\lambda} = 0$ and $\tau = 0$.

The extended imaging condition has two main uses. First, it characterizes wavefield reconstruction errors because, for incorrectly reconstructed wavefields, the crosscorrelation energy does not focus completely at zero lags in space and time. Sources of wavefield reconstruction errors include inaccurate numeric solutions to the wave equation, inaccurate (velocity) models for wavefield reconstruction, inadequate wavefield sampling on the acquisition surface, and uneven illumination of the subsurface. Typically, all of these causes of inaccurate wavefield reconstruction occur simultaneously, and it is difficult to separate them after imaging. Second, assuming accurate wavefield reconstruction, the extended imaging condition can be used for angle decomposition. This leads to representations of reflectivity as a function of angles of incidence and reflection at all points in the imaged volume (Sava and Fomel, 2003). Here, we assume that wavefield reconstruction is accurate and concentrate on further extensions of the imaging condition, such as angle decomposition.

Imaging with vector displacements

When imaging with vector wavefields, the extended imaging condition from equation 8 can be applied directly to the various components of the reconstructed source and receiver wavefields, as with the conventional imaging procedure described earlier. An extended image constructed from vector displacement wavefields is

$$I_{ij}(\mathbf{x},\boldsymbol{\lambda},\tau) = \int u_{si}(\mathbf{x}-\boldsymbol{\lambda},t-\tau)u_{rj}(\mathbf{x}+\boldsymbol{\lambda},t+\tau)dt, \quad (9)$$

where u_{si} and u_{rj} stand for the Cartesian components x,y,z of the vector source and receiver wavefields. This imaging condition suffers from the same drawbacks as the conventional imaging condition applied to the Cartesian components of the reconstructed wavefields, i.e., crosstalk between the unseparated wave modes.

Imaging with scalar and vector potentials

An extended imaging condition can be designed for elastic wavefields decomposed in scalar and vector potentials, just as for the conventional imaging procedure:

$$I_{ij}(\mathbf{x},\boldsymbol{\lambda},\tau) = \int \alpha_{si}(\mathbf{x}-\boldsymbol{\lambda},t-\tau)\alpha_{rj}(\mathbf{x}+\boldsymbol{\lambda},t+\tau)dt, \quad (10)$$

where the α_{si} and α_{rj} stand for the various wave modes $\alpha = \{\mathrm{P},\mathrm{S}\}$ of the source and receiver wave fields, and $\boldsymbol{\lambda}$ and τ stand for crosscorrelation tags in space and time, respectively.

ANGLE DECOMPOSITION

The main uses of images constructed using extended imaging conditions are MVA and AVA analysis. Such analyses, however, require that images be decomposed corresponding to various angles of incidence, a procedure often referred to as angle decomposition. Angle decomposition takes different forms, corresponding to the type of wavefields involved in imaging. Thus, we can distinguish angle decomposition for scalar (acoustic) and vector (elastic) wavefields.

Scalar wavefields

When imaging with the acoustic wave equation, the reflection angle corresponding to incidence and reflection of P-wave mode can be constructed after imaging, using mapping based on the relation (Sava and Fomel, 2005)

$$\tan\theta_a = \frac{|\mathbf{k}_{\boldsymbol{\lambda}}|}{|\mathbf{k}_{\mathbf{x}}|}, \quad (11)$$

where θ_a is the incidence angle and where $\mathbf{k}_{\mathbf{x}} = \mathbf{k}_{\mathbf{r}} - \mathbf{k}_{\mathbf{s}}$ and $\mathbf{k}_{\boldsymbol{\lambda}} = \mathbf{k}_{\mathbf{r}} + \mathbf{k}_{\mathbf{s}}$ are defined using the source and receiver wavenumbers $\mathbf{k}_{\mathbf{s}}$ and $\mathbf{k}_{\mathbf{r}}$. The information required to decompose the reconstructed wavefields as a function of $\mathbf{k}_{\mathbf{x}}$ and $\mathbf{k}_{\boldsymbol{\lambda}}$ is readily available in the images $I(\mathbf{x},\boldsymbol{\lambda},\tau)$, constructed by equation 9 and 10. After angle decomposition, $I(\mathbf{x},\theta,\phi)$ represents a mapping of the image $I(\mathbf{x},\boldsymbol{\lambda},\tau)$ from

offsets to angles. In other words, all information for characterizing angle-dependent reflectivity is available in the image obtained by the extended imaging conditions.

Vector wavefields

A similar approach can be used to decompose reflectivity as a function of incidence and reflection angles for elastic wavefields imaged with equation 9 and 10. The angle θ_e, characterizing the average angle between incidence and reflected rays, can be computed using (Sava and Fomel, 2005)

$$\tan^2\theta_e = \frac{(1+\gamma)^2|\mathbf{k_\lambda}|^2 - (1-\gamma)^2|\mathbf{k_x}|^2}{(1+\gamma)^2|\mathbf{k_x}|^2 - (1-\gamma)^2|\mathbf{k_\lambda}|^2}, \qquad (12)$$

where γ is the velocity ratio of the incident and reflected waves, e.g., V_P/V_S for incident P-mode and reflected S-mode. Figure 1 shows the notations used in equation 12, where $|\mathbf{p_x}| = |\mathbf{k_x}|/\omega$, $|\mathbf{p_\lambda}| = |\mathbf{k_\lambda}|/\omega$, and ω is the angular frequency at the imaging location $\mathbf{x}$. The angle decomposition equation 12 is designed for PS reflections and reduces to equation 11 for PP reflections when $\gamma = 1$.

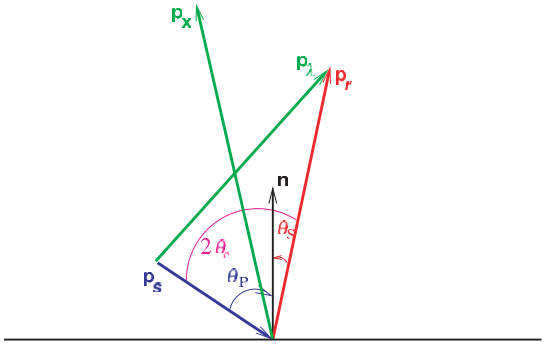

Figure 1. Local wave vectors of the converted wave at a common-image-point location in 3D. The plot shows the conversion in the reflection plane in two dimensions. The labels $\mathbf{p_s}$, $\mathbf{p_r}$, $\mathbf{p_x}$, and $\mathbf{p_\lambda}$ are ray-parameter vectors for the source ray, receiver ray, and combinations of the two. The length of the incidence and reflection wave vectors are inversely proportional to the incidence and reflection wave velocity, respectively. Vector $\mathbf{n}$ is the normal of the reflector. By definition, $\mathbf{p_x} = \mathbf{p_r} - \mathbf{p_s}$ and $\mathbf{p_\lambda} = \mathbf{p_r} + \mathbf{p_s}$.

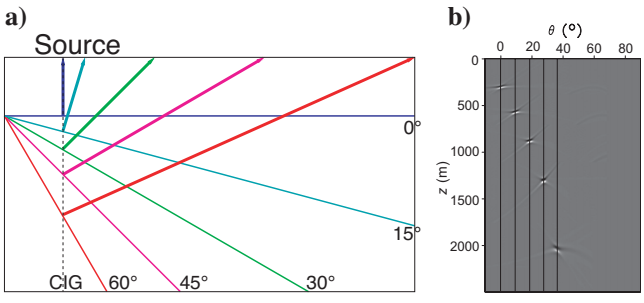

Figure 2. (a) Model showing one shot over multiple reflectors dipping at 0°, 15°, 30°, 45°, and 60°. The vertical dashed line shows a common-image-gather (CIG) location. The incidence ray is vertically down, and P-to-S conversions are marked by arrows pointing away from the reflectors. (b) Converted-wave-angle gather obtained from an algorithm described by Sava and Fomel (2006a). Converted wave angles are always smaller than incidence angles (in this case, the dips of the reflectors) except for normal incidence.

Angle decomposition using equation 12 requires computation of an extended imaging condition with 3D space lags $(\lambda_x, \lambda_y, \lambda_z)$, which is computationally costly. Faster computation can be done if we avoid computing the vertical lag λ_z, in which case the angle decomposition can be done using the expression (Sava and Fomel, 2005)

$$\tan\theta_e = \frac{(1+\gamma)(a_{\lambda_x} + b_x)}{2\gamma k_z + \sqrt{4\gamma^2 k_z^2 + (\gamma^2-1)(a_{\lambda_x} + b_x)(a_x + b_{\lambda_x})}}, \qquad (13)$$

where $a_{\lambda_x} = (1+\gamma)k_{\lambda_x}$, $a_x = (1+\gamma)k_x$, $b_{\lambda_x} = (1-\gamma)k_{\lambda_x}$, and $b_x = (1-\gamma)k_x$.

Figure 2 shows a model of five reflectors and the extracted angle gathers for these reflectors at the source location. For PP reflections, they would occur in the angle gather at angles equal with the reflector slopes. However, for PS reflections, as illustrated in Figure 2, the reflection angles are smaller than the reflector slopes, as expected.

EXAMPLES

We test the imaging conditions with data simulated on a modified subset of the Marmousi2 model (Martin et al., 2002). The section is at the left side of the entire model, which is relatively simple and makes it easier to examine the quality of the images.

Imaging with vector displacements

Consider the images obtained for the model in Figure 3. Figure 3a depicts the P-wave velocity (smooth function between 1.6 and 3.2 km/s), and Figure 3b shows the density (variable between 1 and 2 g/cm^3). The S-wave velocity is a scaled version of the P-wave velocity, with $V_P/V_S = 2$. Data are modeled and migrated in the smooth velocity background to avoid backscattering, and the migration density is constant throughout the model. We smooth the velocity background for modeling and migration, and we use density discontinuities to generate reflections in modeling but use a constant density in migration. The smooth velocity background for modeling and migration avoids backscattering during wavefield reconstruction.

The elastic data (Figure 4a and b) are simulated using a space-time staggered-grid finite-difference solution to the isotropic elastic wave equation (Virieux, 1984, 1986; Mora, 1987, 1988). We simulate data for a source located at $x = 6.75$ km and $z = 0.5$ km. Because we are using an explosive source and the background velocity is smooth, the simulated wavefield is represented mainly by P-wave incident energy and the receiver wavefield is represented by a combination of P- and S-wave reflected energy. The data contain a mix of P- and S-wave modes, as can be seen by comparing the vertical and horizontal displacement components (Figure 4a and b) with the separated P- and S-wave modes (Figure 4c and d).

Imaging the data shown in Figure 4a and b using the imaging condition from equation 3, we obtain the images in Figure 5. Figure 5a-d corresponds to the crosscorrelation of the z- and x-components of the source wavefield with the z- and x-components of the receiver wavefield. The input data do not represent separated wave modes, so the images produced with the imaging condition based on vector displacements do not separate PP and PS reflectivity. Thus, the images are hard to interpret because it is unclear what incident and reflected

wave modes the reflections represent. In reality, reflections corresponding to all wave modes are present in all panels.

Imaging with scalar and vector potentials

Consider the images (Figure 6) obtained for using the imaging condition from equation 7 applied to the data (Figure 4a and b) from the preceding example. Because we used an explosive source for our simulation, the source wavefield contains mostly P-wave energy but the receiver wavefield contains P- and S-wave mode energy. Helmholtz decomposition after extrapolation but prior to imaging isolates P- and S-wavefield components. Therefore, migration produces images of reflectivity corresponding to PP and PS reflections (Figure 6a and b) but not reflectivity corresponding to SP or SS reflections (Figure 6c and d). The illumination regions are different between PP and PS images because of different illumination angles of the two propagation modes for the given acquisition geometry. The PS image (Figure 6b) also shows the usual polarity reversal for positive and negative angles of incidence measured relative to the reflector normal.

By comparing Figure 6a and b with Figure 5a and b, it is apparent that the crosstalk in the images obtained from displacement-based imaging conditions is more prominent than that obtained from potential-based imaging conditions, especially in Figure 5a. Furthermore, the polarity in Figure 5b, normally taken as the PS image, does not reverse polarity at normal incidence, which is incorrect.

Angle decomposition

Figures 5 and 6 correspond to the conventional imaging conditions from equations 3 and 7. We can construct other images using the extended imaging conditions from equations 9 and 10, which can be used for angle decomposition after imaging. Then we can use equation 13 to compute angle gathers from horizontal space cross-correlation lags.

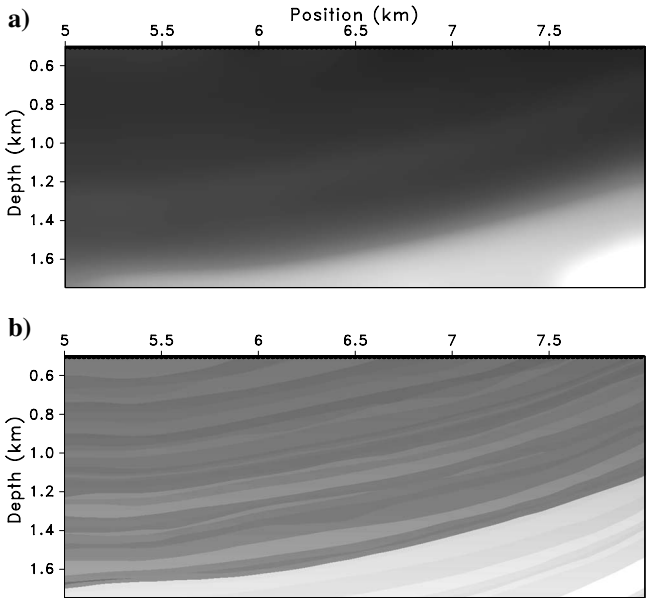

Figure 3. (a) P- and S-wave velocity models and (b) density model used for isotropic elastic wavefield modeling, where V_P ranges from 1.6 to 3.2 km/S from top to bottom and where $V_P/V_S = 2$; density ranges from 1 to 2 g/cm^3.

Figure 7 shows the PP and PS horizontal lags and angle gathers for the common image gather (CIG) location in the middle of the reflectivity model, given a single source at $x = 6.75$ km and $z = 0.5$ km. PP and PS horizontal lags are lines dipping at angles equal to the incidence angles (real incidence angles for PP reflection and average of incidence and reflection angles for PS reflection) at the CIG location. The PP angles are larger than PS angles at all reflectors, as illustrated on the simple synthetic example in Figure 2.

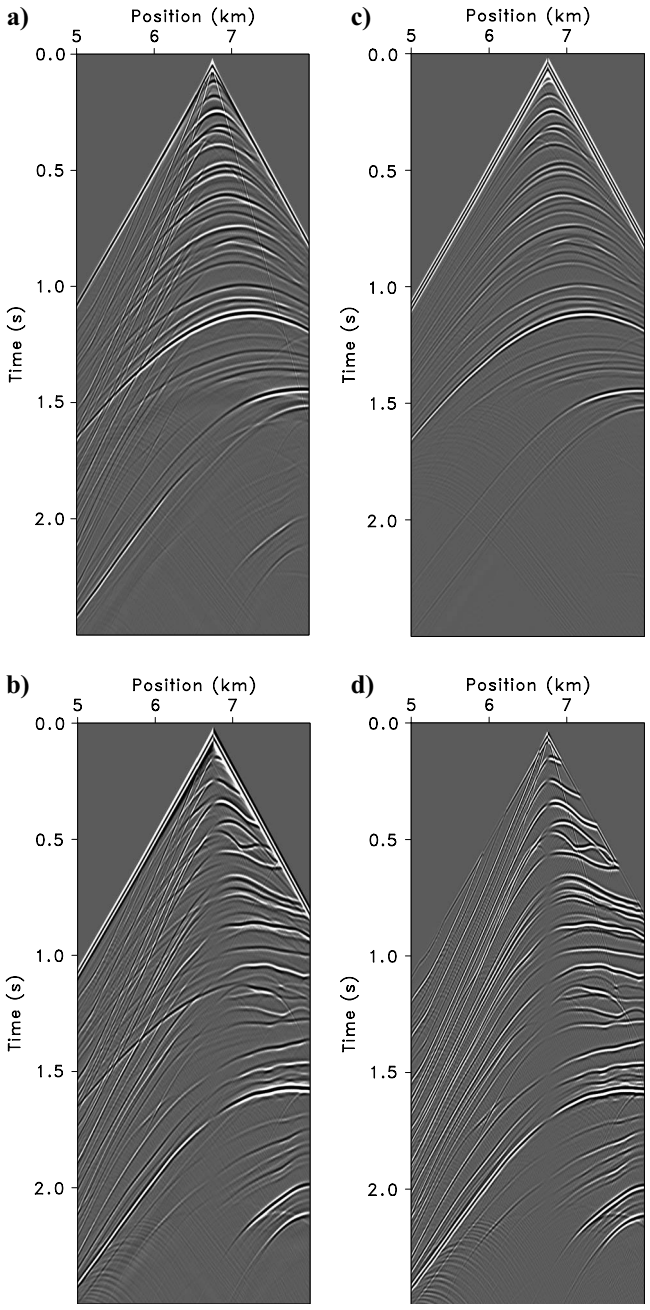

Figure 4. Elastic data simulated in Figure 3 with a source at $x = 6.75$ km and $z = 0.5$ km and receivers at $z = 0.5$ km: (a) vertical component, (b) horizontal component, (c) scalar potential, and (d) vector potential of the elastic wavefield. Vertical (a) and horizontal (b) components contain a mix of P- and S-modes, as seen by comparison with panels (c) and (d).

Figure 8 shows the PP and PS horizontal lags and angle gathers for the same CIG location, given many sources from $x = 5.5$ to 7.5 km and $z = 0.5$ km. The horizontal-space crosscorrelation lags are focused around $\lambda = 0$, which justifies the use of conventional imaging condition extracting the crosscorrelation of the source and receiver wavefields at zero lag in space and time. Thus, the zero lag of the images obtained by the extended imaging condition represents the image at the particular CIG location. The PP and PS gathers for many

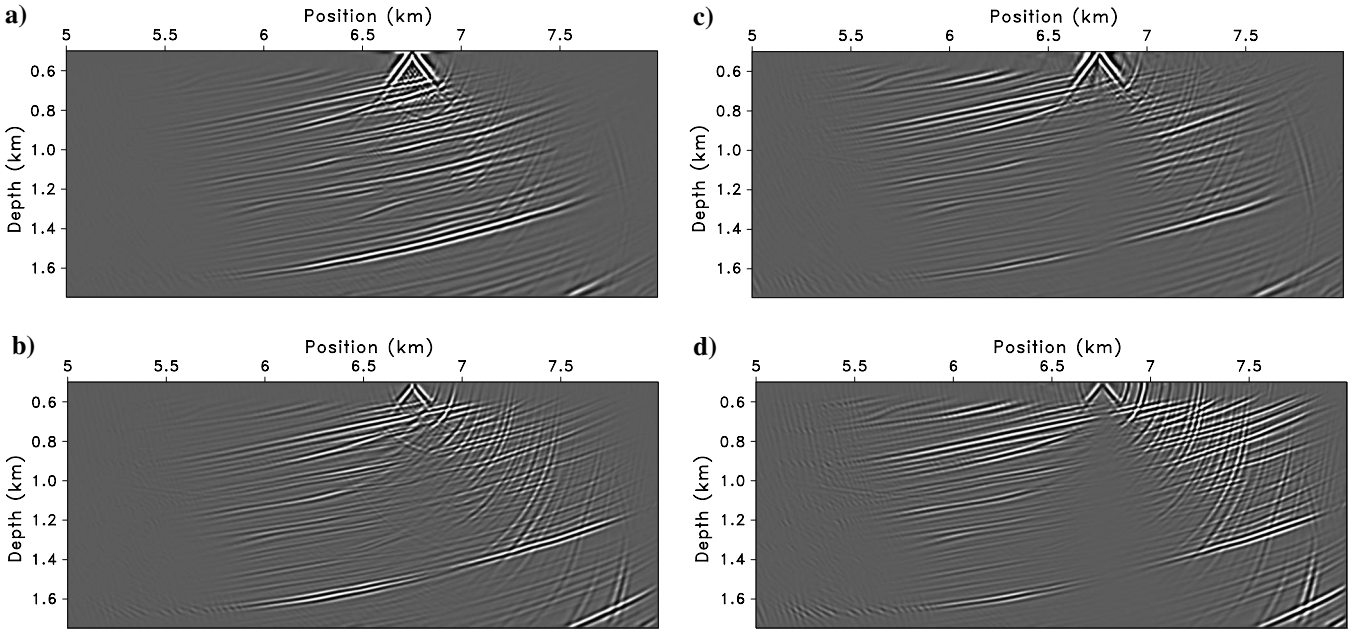

Figure 5. Images produced with the displacement-component imaging condition from equation 3. Panels (a), (b), (c), and (d) correspond to the crosscorrelation of the vertical and horizontal components of the source wavefield with the vertical and horizontal components of the receiver wavefield, respectively. Images (a) to (d) are the zz, zx, xz, and xx components respectively. The image corresponds to one shot at $x = 6.75$ km, $z = 0.5$ km. Receivers are located at all locations at $z = 0.5$ km.

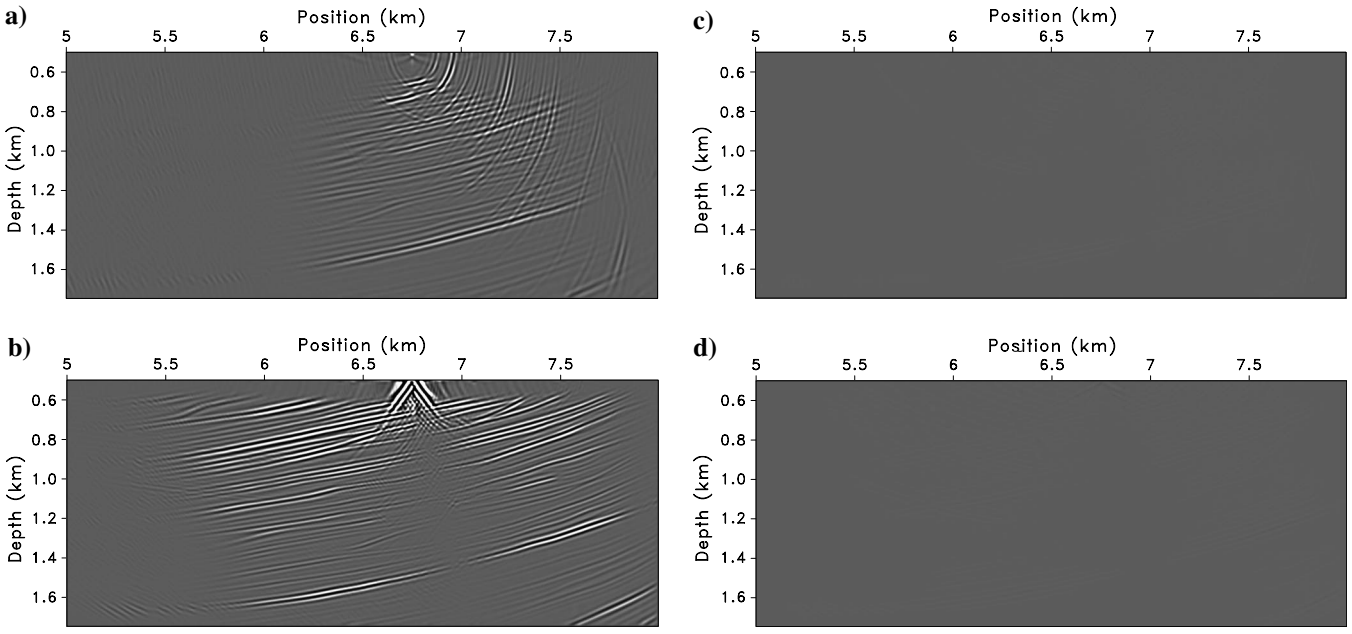

Figure 6. Images produced with the scalar and vector potentials imaging condition from equation 7. Panels (a), (b), (c), and (d) correspond to the crosscorrelation of the P and S components of the source wavefield with P and S components of the receiver wavefield respectively. Images (a) to (d) are the PP, PS, SP, and SS components, respectively. The image corresponds to one shot at position $x = 6.75$ km and $z = 0.5$ km. Receivers are located at all locations at $z = 0.5$ km. Panels (c) and (d) are blank because an explosive source was used to generate synthetic data.

sources are flat because the migration was done with correct migration velocity. The PS angle gather (Figure 8d) shows a polarity reversal at $\theta = 0$, which is consistent with the fact that PS images change polarity at normal incidence as expected.

DISCUSSION

Our presentation of the angle-domain RTM method deliberately ignores several practical challenges to focus on the elastic imaging condition. However, for completeness, a few issues in conjunction with the imaging condition should be addressed as we design a practical method for elastic RTM.

First, reconstructing the receiver wavefield requires that the multicomponent recorded data be injected into the model in reverse time. In other words, the recorded data act as displacement sources at receiver positions. In elastic materials, displacement sources trigger compressional and transverse wave modes, no matter what portion of the recorded elastic wavefield is used as a source. For example, injecting a recorded compressional mode triggers a compressional (physical) mode and a transverse (nonphysical) mode in the subsurface. Both modes propagate in the subsurface and might correlate with wave modes from the source side. There are several ways to address this problem, such as imaging in the angle domain where the nonphysical modes appear as events with nonflat moveout. We can make an analogy between those nonphysical waves and multiples that also lead to nonflat events in the angle domain. Thus, the source injection artifacts might be eliminated by filtering the migrated images in the angle domain, similar to the technique used by Sava and Guitton (2005) to suppress multiples after imaging.

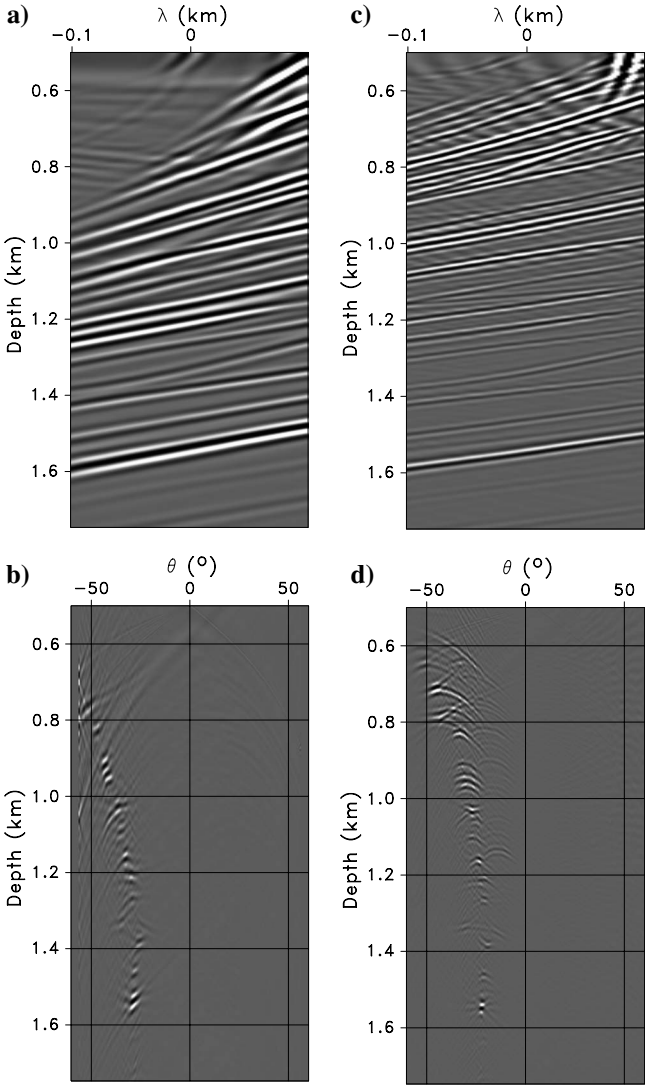

Figure 7. Horizontal crosscorrelation lags for (a) PP and (c) PS reflections for the model in Figure 3a and b. The source is at $x = 6.75$ km, and the CIG is located at $x = 6.5$ km. (b) PP and (d) PS angle gathers decomposed from the horizontal lag gathers in views (a) and (c), respectively. As expected, PS angles are smaller than PP angles for a particular reflector as a result of smaller reflection angles.

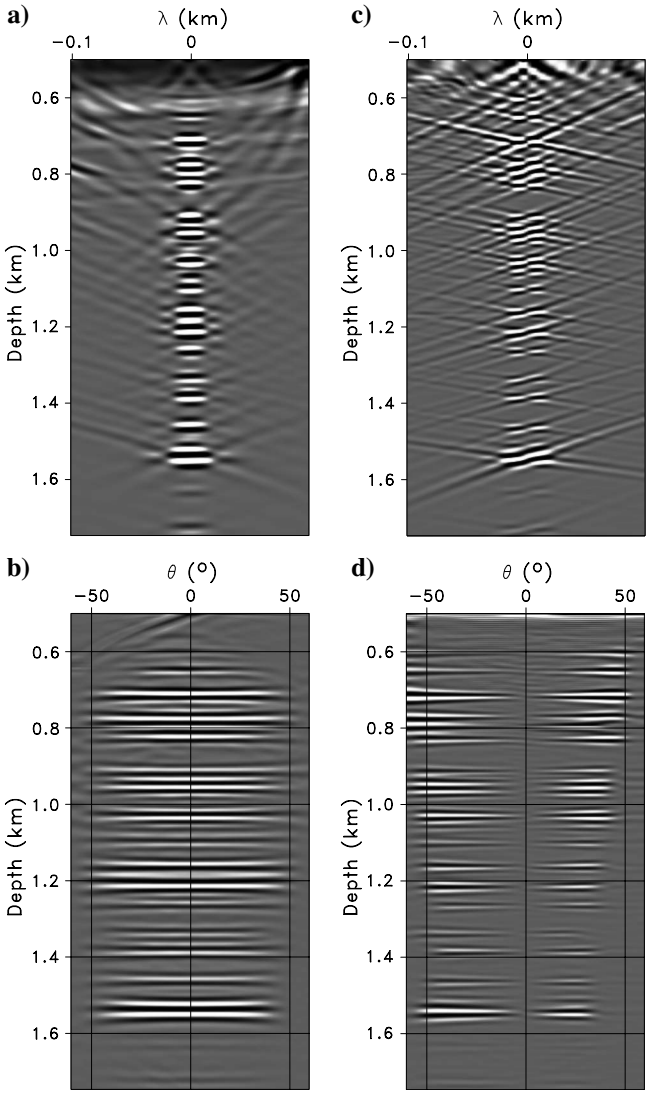

Figure 8. Horizontal crosscorrelation lags for (a) PP and (c) PS reflections for the model in Figure 3a and b. These CIGs correspond to 81 sources from $x = 5.5$ to 7.5 km at $z = 0.5$ km. The CIG is located at $x = 6.5$ km. (b) PP and (d) PS angle gathers decomposed from the horizontal lag gathers in views (a) and (c), respectively. The velocity used for imaging is correct, so the PP and PS gathers are flat. The PP angle gathers do not change polarity at normal incidence, but the PS angle gathers do.

Second, the data recorded at a free surface contain both up- and downgoing waves. Ideally, we should use only upgoing waves as a source for reconstructing the elastic wavefields by time reversal. In our examples, we assume an absorbing surface to avoid this additional complication and concentrate on the imaging condition. However, practical implementations require directional separation of waves at the surface (Wapenaar and Haimé, 1990; Wapenaar et al., 1990; Admundsen and Reitan, 1995; Admundsen et al., 2001; Hou and Marfurt, 2002). Furthermore, a free surface allows other wave modes to be generated in the process of wavefield reconstruction using the elastic wave equation, e.g., Rayleigh and Love waves. Although those waves do not propagate deep into the model, they might interfere with the directional wavefield separation at the surface.

Third, we suggest that angle-dependent reflectivity constructed using extended imaging conditions might allow for elastic AVA analysis. This theoretical possibility requires that the wavefields be reconstructed correctly in the subsurface to account for accurate amplitude variation. For example, boundaries between regions with different material properties need to be located reasonably in the subsurface to generate correct mode conversions, and the radiation pattern of the source needs to be known. Neither of these aspects is part of our analysis, but they represent important considerations for practical elastic wavefield imaging.

Fourth, the wave-mode separation using divergence and curl operators, as required by Helmholtz decomposition, does not work well in elastic anisotropic media. Anisotropy requires that the separation operators account for the local anisotropic parameters that may vary spatially (Yan and Sava, 2008). However, we do not discuss anisotropic wave-mode decomposition but restrict our attention to angle-domain imaging in isotropic models.

CONCLUSIONS

We have presented a method for RTM with angle-domain imaging formulated for multicomponent elastic data. The method is based on separating elastic wavefields reconstructed in the subsurface into pure wave modes using conventional Helmholtz decomposition. Elastic wavefields from the source and receivers are separated into pure compressional and transverse wave modes, which are then used for angle-domain imaging. The images formed using this procedure are interpretable in terms of subsurface physical properties, for example, by analyzing the PP or PS angle-dependent reflectivity. In contrast, images formed by simple crosscorrelation of Cartesian components of reconstructed elastic wavefields mix contributions from P and S reflections and are harder to interpret. Artifacts caused by backpropagating the recorded data with displacement sources are present in both types of images, although they are easier to distinguish and attenuate on the images constructed with pure elastic wave modes separated prior to imaging.

The method is advantageous because it forms images with clearer physical meaning and is based on more accurate physics of wave propagation in elastic materials. For example, this methodology allows for wave-mode conversions in wavefield reconstruction. This contrasts with alternative methods for multicomponent imaging that separate wave modes on the surface and then image those independently. In addition, elastic images can be formed in the angle domain using extended imaging conditions, which offers the potential for MVA and AVA analysis.

ACKNOWLEDGMENTS

We acknowledge the support of the sponsors of the Center for Wave Phenomena at Colorado School of Mines. We also acknowledge GEOPHYSICS Associate Editor John Etgen and reviewers Dan Whitmore, Jim Gaiser, and Paul Fowler, whose comments and suggestions significantly improved the manuscript.

REFERENCES

Admundsen, L., L. Ikelle, and L. Berg, 2001, Multidimensional signature deconvolution and free surface multiple elimination of marine multicomponent ocean-bottom seismic data: Geophysics, **66**, 1594–1604.
Admundsen, L., and A. Reitan, 1995, Decomposition of multicomponent sea-floor data into upgoing and downgoing P- and S-waves: Geophysics, **60**, 560–572.
Aki, K., and P. Richards, 2002, Quantitative seismology, 2nd ed.: University Science Books.
Alford, R. M., K. R. Kelly, and D. M. Boore, 1974, Accuracy of finite-difference modeling of the acoustic wave equation: Geophysics, **39**, 834–842.
Baysal, E., D. D. Kosloff, and J. W. C. Sherwood, 1983, Reverse time migration: Geophysics, **48**, 1514–1524.
Boechat, J. B., A. Bulcão, D. M. S. Filho, P. M. Cunha, W. J. Mansur, and T. Moreira, 2007, A 3D reverse-time migration scheme for offshore seismic data: 77th Annual International Meeting, SEG, Expanded Abstracts, 2427–2431.
Bolt, B. A., and W. D. Smith, 1976, Finite-element computation of seismic anomalies for bodies of arbitrary shape (short note): Geophysics, **41**, 145–151.
Chang, W. F., and G. A. McMechan, 1986, Reverse-time migration of offset vertical seismic profiling data using the excitation-time imaging condition: Geophysics, **51**, 67–84.
——, 1994, 3-D elastic prestack, reverse-time depth migration: Geophysics, **59**, 597–609.
Claerbout, J. F., 1971, Toward a unified theory of reflector mapping: Geophysics, **36**, 467–481.
——, 1985, Imaging the earth's interior: Blackwell Scientific Publications.
Clayton, R. W., 1981, Wavefield inversion methods for refraction and reflection data: Ph.D. dissertation, Stanford University.
Clayton, R. W., and D. Brown, 1979, The choice of variables for elastic wave extrapolation: SEP Report 20, 73–96.
Cunha Filho, C., 1992, Elastic modeling and migration in earth models: Ph.D. dissertation, Stanford University.
Dablain, M. A., 1986, The application of high-order differencing to the scalar wave equation: Geophysics, **51**, 54–66.
Dai, N., and S. Cheadle, 1996, Pseudo-spectral migration in the f-x domain: 66th Annual International Meeting, SEG, Expanded Abstracts, 427–430.
Dellinger, J., and J. Etgen, 1990, Wavefield separation in two-dimensional anisotropic media (short note): Geophysics, **55**, 914–919.
Etgen, J. T., 1988, Prestacked migration of P and SV-waves: 58th Annual International Meeting, SEG, Expanded Abstracts, 972–975.
Fomel, S., and M. M. Backus, 2003, Multicomponent seismic data registration by least squares: 73rd Annual International Meeting, SEG, Expanded Abstracts, 781–784.
Gaiser, J., 1996, Multicomponent V_P/V_S correlation analysis: Geophysics, **61**, 1137–1149.
Gaiser, J., N. Moldoveanu, C. Macbeth, R. Michelena, and S. Spitz, 2001, Multicomponent technology: The players, problems, applications, and trends: Summary of the workshop sessions: The Leading Edge, **20**, 974–977.
Gray, S. H., J. Etgen, J. Dellinger, and D. Whitmore, 2001, Seismic migration problems and solutions: Geophysics, **66**, 1622–1640.
Hokstad, K., 2000, Multicomponent Kirchhoff migration: Geophysics, **65**, 861–873.
Hokstad, K., R. Mittet, and M. Landro, 1998, Elastic reverse time migration of marine walkaway vertical seismic profiling data: Geophysics, **63**, 1685–1695.
Hou, A., and K. Marfurt, 2002, Multicomponent prestack depth migration by scalar wavefield extrapolation: Geophysics, **67**, 1886–1894.
Jones, I. F., M. C. Goodwin, I. D. Berranger, H. Zhou, and P. A. Farmer, 2007, Application of anisotropic 3D reverse time migration to complex North Sea imaging: 77th Annual International Meeting, SEG, Expanded Abstracts, 2140–2144.
Knapp, S., N. Payne, and T. Johns, 2001, Imaging through gas clouds: A case history from the Gulf of Mexico: 71st Annual International Meeting, SEG, Expanded Abstracts, 776–779.
Kuo, J. T., and T. F. Dai, 1984, Kirchhoff elastic wave migration for the case of noncoincident source and receiver: Geophysics, **49**, 1223–1238.

Levin, S. A., 1984, Principle of reverse-time migration: Geophysics, **49**, 581–583.
Li, X.-Y., 1998, Fracture detection using P-P and P-S waves in multicomponent sea-floor data: 68th Annual International Meeting, SEG, Expanded Abstracts, 2056–2059.
Martin, G. S., K. J. Marfurt, and S. Larsen, 2002, Marmousi-2: An updated model for the investigation of AVO in structurally complex areas: 72nd Annual International Meeting, SEG, Expanded Abstracts, 1979–1982.
McMechan, G. A., 1982, Determination of source parameters by wavefield extrapolation: Geophysical Journal International, **71**, 613–628.
———, 1983, Migration by extrapolation of time-dependent boundary values: Geophysical Prospecting, **31**, 413–420.
Mora, P., 1988, Elastic wave-field inversion of reflection and transmission data: Geophysics, **53**, 750–759.
———, 1987, Nonlinear two-dimensional elastic inversion of multioffset seismic data: Geophysics, **52**, 1211–1228.
Nickel, M., and L. Sonneland, 2004, Automated PS to PP event registration and estimation of a high-resolution V_P-V_P ratio volume: 74th Annual International Meeting, SEG, Expanded Abstracts, 869–872.
Pestana, R. C., F. M. R. da Mota, T. J. Ulrych, S. Freire, and F. B. da Silva, 1989, Deterministic and stochastic separation of P- and SV-waves: A comparison: 59th Annual International Meeting, SEG, Expanded Abstracts, 1308–1311.
Sava, P., and S. Fomel, 2003, Angle-domain common image gathers by wavefield continuation methods: Geophysics, **68**, 1065–1074.
———, 2005, Wave-equation common-angle gathers for converted waves: 75th Annual International Meeting, SEG, Expanded Abstracts, 947–950.
———, 2006a, Time-shift imaging condition for converted waves: 76th Annual International Meeting, SEG, Expanded Abstracts, 2460–2464.
———, 2006b, Time-shift imaging condition in seismic migration: Geophysics, **71**, no. 6, S209–S217.
Sava, P., and A. Guitton, 2005, Multiple attenuation in the image space: Geophysics, **70**, no. 1, V10–V20.
Seriani, G., and E. Priolo, 1991, High-order spectral element method for acoustic wave modeling: 71st Annual International Meeting, SEG, Expanded Abstracts, 1561–1564.
Seriani, G., E. Priolo, J. Carcione, and E. Padovani, 1992, High-order spectral element method for elastic wave modeling: 62nd Annual International Meeting, SEG, Expanded Abstracts, 1285–1288.
Simmons, J., and M. Backus, 2003, An introduction — Multicomponent: The Leading Edge, **22**, 1227–1262.
Stewart, R. R., J. E. Gaiser, R. J. Brown, and D. C. Lawton, 2003, Converted-wave seismic exploration: Applications: Geophysics, **68**, 40–57.
Sun, R., G. A. McMechan, C.-S. Lee, J. Chow, and C.-H. Chen, 2006, Prestack scalar reverse-time depth migration of 3D elastic seismic data: Geophysics, **71**, no. 5, S199–S207.
Virieux, J., 1984, SH-wave propagation in heterogeneous media: Velocity-stress finite-difference method: Geophysics, **49**, 1933–1942.
———, 1986, P-SV wave propagation in heterogeneous media: Velocity-stress finite-difference method: Geophysics, **51**, 889–901.
Wapenaar, C. P. A., and G. C. Haimé, 1990, Elastic extrapolation of seismic P- and S-waves: Geophysical Prospecting, **38**, 23–60.
Wapenaar, C. P. A., P. Herrmann, D. J. Verschuur, and A. J. Berkhout, 1990, Decomposition of multicomponent seismic data into primary P- and S-wave responses: Geophysical Prospecting, **38**, 633–661.
Wapenaar, C. P. A., N. A. Kinneging, and A. J. Berkhout, 1987, Principle of prestack migration based on the full elastic two-way wave equation: Geophysics, **52**, 151–173.
Whitmore, N. D., 1983, Iterative depth migration by backward time propagation: 53rd Annual International Meeting, SEG, Expanded Abstracts, 382–385.
———, 1995, An imaging hierarchy for common-angle seismograms: Ph.D. dissertation, The University of Tulsa.
Yan, J., and P. Sava, 2008, Elastic wavefield separation for VTI media: 78th Annual International Meeting, SEG, Expanded Abstracts, 2245–2249.
Zhe, J., and S. A. Greenhalgh, 1997, Prestack multicomponent migration: Geophysics, **62**, 598–613.
Zhu, X., S. Altan, and J. Li, 1999, Recent advances in multicomponent processing: The Leading Edge, **18**, 1283–1288.